# Development of Triphenylamine Derived Photosensitizers for Efficient Hydrogen Evolution from Water

*Yudong Wen[a], Linyu Fan[a], Xiao Yao[a,b*], Cheuk-Lam Ho[a*]*

[a] *Department of Applied Biology and Chemical Technology, The Hong Kong Polytechnic University, Hung Hom, Hong Kong, P. R. China; PolyU Shenzhen Research Institute, Shenzhen, P. R. China*
*Email: cheuk-lam.ho@polyu.edu.hk*
[b] *School of Ecological Environment and Urban Construction, Fujian University of Technology, Fuzhou 350118, China.*

ORCID
Yudong Wen: 0000-0002-1368-1402
Linyu Fan: 0000-0003-1812-3781
Xiao Yao: 0000-0002-0085-4861
Cheuk-Lam Ho: 0000-0001-8596-0307

**Abstract**

A series of new (donor)$_2$-donor-π-acceptor ($D_2$-D-π-A) and (acceptor)$_2$-donor-π-acceptor ($A_2$-D-π-A) organic photosensitizers based on the framework of (Z)-2-cyano-3-(5-(4-(diphenylamino)phenyl)thiophen-2-yl)acrylic acid have been synthesized and characterized. By incorporating groups with different electron-donating or withdrawing abilities, such as dibenzothiophene (DBT), dibenzofuran (DBF), and triazine (TA), into the triphenylamine segment, their photophysical properties have been regulated. Theoretical calculations were used to explore how various donor-acceptor combinations influence their hydrogen production performance. Notably, **DBF-CN** achieved the highest turnover number (TON) of 10,202 and an initial turnover frequency ($TOF_i$) of 151.6 $h^{-1}$ under green light irradiation, with an initial activity ($Activity_i$) of 113,532 μmol $g^{-1}$ $h^{-1}$ and an apparent quantum yield ($AQY_i$) of 0.76%. This dye-sensitized-$TiO_2$-Pt system is recognized as one of the most efficient and durable systems for photocatalytic hydrogen production under green light irradiation, as described in the literature, when compared using TOF and TON values. Experimental results indicate that the $D_2$-D-π-A system significantly enhances photocatalytic hydrogen evolution (PHE) performance more effectively than the $A_2$-D-π-A system, while also maintaining stability under prolonged light exposure.

Keywords: Photocatalysis; Organic Photosensitizers; Hydrogen; Triphenylamine; Donor-Acceptor

## 1. Introduction

The unremitting exploration of new energy sources has caused hydrogen to be highly regarded as a clean and sustainable energy alternative [1,2]. Due to its remarkable energy density and environmental compatibility, hydrogen is already considered one of the most promising energy sources for future development [3]. Among the various methods for hydrogen production, photocatalytic water-splitting has garnered significant attention since the discovery of the Honda-Fujishima effect in 1972 [4]. This technology fully utilizes abundant natural resources and generates hydrogen without releasing greenhouse gases, rendering it an exceptionally appealing solution in the energy sector [5].

The photocatalyst plays a pivotal role in the process of photocatalytic hydrogen generation from water, as it is primarily responsible for absorbing light energy and initiating the generation of excitons [6,7]. Among various metal oxides, titanium dioxide ($TiO_2$) is widely used due to its outstanding chemical stability, affordability, and non-toxic nature. However, $TiO_2$ has a wide bandgap of approximately 3.2 eV, which limits its absorption to ultraviolet light [8]. This significantly restricts its effectiveness within the visible light range. To address these limitations, we drew inspiration from dye-sensitized solar cells by attaching molecular photosensitizers (PSs) to $TiO_2$ and further modifying their molecular conjugated structures. This modification enhances the molar extinction coefficient (ε) and improves charge transfer capabilities of the photocatalyst. As a result, the photocatalyst can more effectively absorb visible light, facilitating the separation and transportation of photogenerated electron-hole pairs, ultimately boosting overall photocatalytic efficiency [9–11]. When designing metal-free organic PS, a donor-π-acceptor (D-π-A) bridging system is commonly employed. This connection effectively facilitates charge separation and transfer, consequently boosting the efficiency of photocatalytic conversion. However, in dye-sensitized systems with "D-π-A" configuration of PSs, dye aggregation and charge recombination often become limiting factor[12]. Such aggregation can reduce energy transfer efficiency and increase the likelihood of charge recombination, thus diminishing photocatalytic performance.

Consequently, researchers are exploring various strategies to inhibit dye aggregation, such as incorporating steric hindrance through molecular design or enhancing molecular charge transfer properties, to optimize the overall performance of photocatalysis[13–15].

Triphenylamine derivatives are widely used as electron donor groups in PSs due to their well-known electron-rich properties and distinctive propeller-like structure[16]. Modifying the triphenylamine structure with suitable heterocyclic groups can enhance its charge separation and transfer capabilities while reducing the likelihood of charge recombination. This improvement occurs because the lone electron pairs on heterocyclic groups can effectively delocalize the charge of photo-oxidized dyes [17]. Dibenzothiophene (DBT), dibenzofuran (DBF), and triazine (TA) compounds are common and important heterocyclic compounds with rigid coplanar structures, extensively used in organic light-emitting diodes (OLEDs), dye-sensitized solar cells (DSSCs) and nonlinear optical materials [18–20].

Here, we propose two types of mono-anchoring organic PSs with either $D_2$-D-π-A or $A_2$-D-π-A molecular framework (**Figure 1**). By incorporating groups with varying electron-donating or electron deficiency into the triphenylamine moiety, the distribution of frontier molecular orbitals of PSs can be regulated. DBT and DBF are used as moderate electron-donating groups to further modify triphenylamine, enhancing its electron-rich properties and intramolecular charge transfer capability in a $D_2$-D-π-A structure. In contrast, triazine groups are used to modify the triphenylamine structure, forming an $A_2$-D-π-A structure to examine the electron-withdrawing effects on triphenylamine's electron-rich segment. The extension of the conjugated structure of triphenylamine expands its absorption spectrum into the visible light region. This expansion efficiently enhances the intramolecular charge transfer of the resulting PSs. The highly twisted and rotational structure of triphenylamine also effectively suppresses π-π stacking and reduces charge transfer resistance. The PSs with electron-rich donor segments, DBT and DBF, demonstrate long-term stability and superior hydrogen production efficiency under prolonged irradiation. Under green LED light

irradiation, **DBF-CN** achieved a turnover number (TON) up to 10,202 over 258 hours, producing 15.3 mL of hydrogen. In contrast, **DTA-CN** produced only 5.2 mL of hydrogen, yielding less than half the amount produced by both **DBT-CN** and **DBF-CN**. To uncover the underlying mechanisms, we systematically examined the relationship between the photophysical properties of the molecules, theoretical calculations, and the efficiency of photocatalytic hydrogen production.

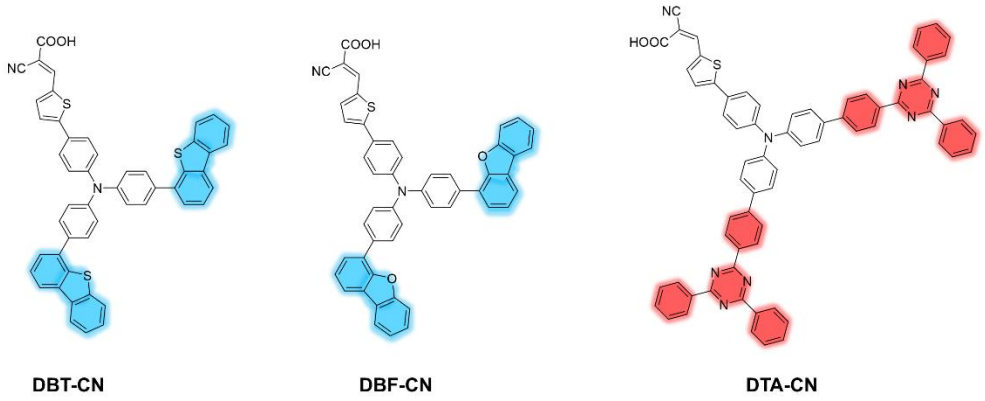


**Figure 1.** The molecular structures of **DBT-CN**, **DBF-CN** and **DTA-CN**.

## 2. Results and Discussion

### 2.1 Synthesis and Characterization

**Scheme 1** outlines the synthetic route for the desired PSs, **DBT-CN**, **DBF-CN** and **DTA-CN**. Initially, a Suzuki reaction is performed to couple 2-formylthiophene with triphenylamine. This is followed by a Wohl-Ziegler reaction to brominate the para position of the nitrogen atom in triphenylamine. Another Suzuki reaction is then conducted to couple with dibenzothiophene, dibenzofuran, or 2,4,6-triphenyltriazine. Finally, a Knoevenagel condensation with cyanoacetic acid is carried out in the presence of piperidine to obtain the target PSs.

Unless previously reported, all organic precursors were characterized using $^{1}H$ and $^{13}C$ NMR spectroscopy (**Figures S1-S17**). A singlet peak observed around δ9.87 ppm corresponds to the proton of the aldehyde precursor. The target organic PSs are soluble in common solvents such as dichloromethane, dimethyl sulfoxide, and tetrahydrofuran. They were characterized using electrospray ionization quadrupole time-of-flight mass spectrometry (ESI-TOF-MS) and $^{1}H$ NMR spectroscopy. The specific downfield singlet peak observed around δ8.5 ppm in the $^{1}H$ NMR spectrum indicates the presence of the carbon-carbon double bond in cyanoacetic acid. The disappearance of the peak at δ9.87 ppm and the appearance of the peak at δ8.5 ppm confirm the successful execution of the final Knoevenagel condensation, indicating the conversion of the aldehyde to cyanoacetic acid. However, obtaining high-quality $^{13}C$ NMR spectra of the PSs proved challenging due to their partial solubility in common organic solvents.

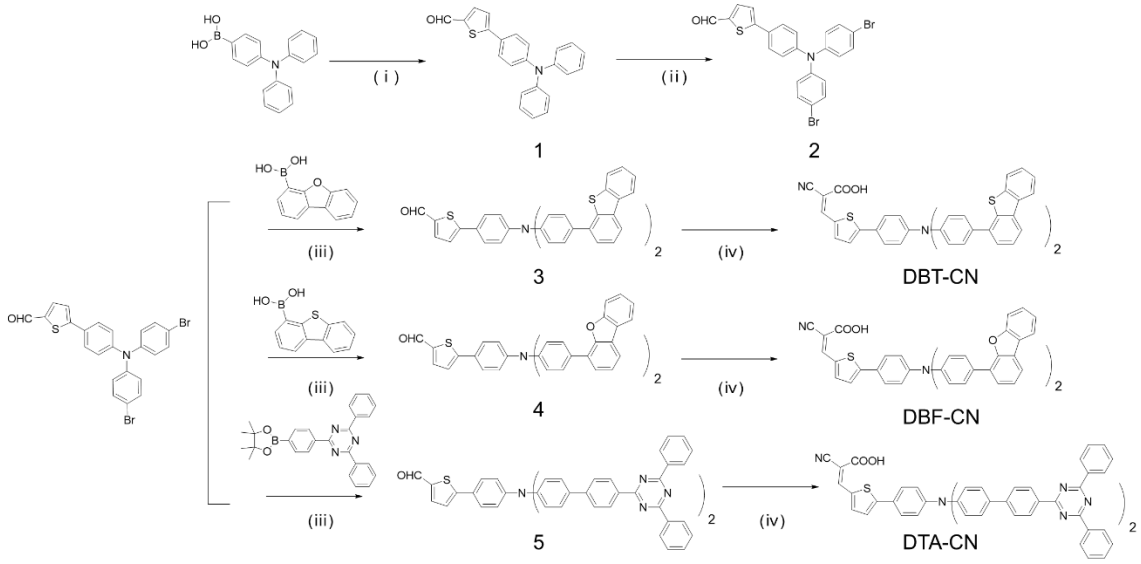


**Scheme 1.** Synthesis of **DBT-CN**, **DBF-CN** and **DTA-CN**: i) 5-Bromothiophene-2-carbaldehyde, $Pd(PPh_3)_4$, THF, $K_2CO_3$ (aq); ii) NBS, dry DMF; iii) $Pd(PPh_3)_4$, THF, $K_2CO_3$ (aq); iv) piperidine, cyanoacetic acid, dry chloroform.

### 2.2 Theoretical calculation

Theoretical simulations using Density Functional Theory (DFT) at the B3LYP/6-31g(d) level were employed to calculate the molecular structures and properties of **DBT-CN**, **DBF-CN**, and **DTA-CN**, as well as their optimized geometries and electrostatic potential surfaces (EPS). As shown in **Figures 2** and **3**, these compounds exhibit relatively twisted conformations in the thiophene and triphenylamine coupling segments, with torsion angles $\theta_1$ around 31.3° and $\theta_2$ and $\theta_3$ within 35°, indicating a significant degree of π-conjugation, which is crucial for facilitating intramolecular charge transfer. The enhanced π-conjugation improves electronic transfer across the molecules, which is essential for their function as PSs in photocatalytic applications. The presence of rotatable saturated carbon-carbon single bonds between triphenylamine and the DBT, DBF, TA or thiophene rings leads to non-planar structures. The distribution of frontier molecular orbitals (FMOs) reveals that the highest occupied molecular orbital (HOMO) is primarily localized on the triphenylamine-thiophene region, with slight delocalization onto the modified DBT and DBF groups. In contrast, the lowest unoccupied molecular orbital (LUMO) is delocalized over the thiophene-cyanoacrylic acid anchoring acceptor. Notably, in the HOMO-1 orbital, the electron cloud is concentrated on the DBT and DBF groups, highlighting their role in

modulating the electronic properties of the molecule. The electrostatic potential surface (EPS) maps further illustrate charge distribution, highlighting regions of electron density and potential sites for chemical interactions. Cyano and carboxyl groups induce substantial electrostatic potential differences, effectively attracting proton accumulation, which is a crucial factor in photocatalytic hydrogen production. The DBT and DBF moieties exhibit weak acceptor properties compared to the electron-rich nature of triphenylamine, which allows them to partially extract local electrons and modulate the molecule's electronic properties. In contrast, the triphenyl triazine group, characterized by a more negative electrostatic potential around the nitrogen atom, demonstrates strong acceptor properties. It effectively extracts local electrons from triphenylamine, thereby promoting the separation and migration of photogenerated charge carriers, which is essential for enhancing photocatalytic efficiency. These findings suggest that introducing electron-rich groups of varying degrees into triphenylamine can establish distinct electron transport pathways within the PSs, leading in differences in hydrogen production capabilities. This positions these materials as promising candidates for solar energy conversion and storage applications. By strategically tailoring the electronic properties through molecular design, it is possible to optimize the performance of these materials for specific applications.

To gain a deeper understanding of the characteristics of excited states, Natural Transition Orbital (NTO) calculations were performed using DBT/DBF/DTA donor fragments as Fragment 1 (F1) and a thiophene anchoring unit as Fragment 2 (F2). These calculations were supplemented by Inter-Fragment Charge Transfer (IFCT) analysis to investigate the excited state properties of the compounds **DBT-CN**, **DBF-CN**, and **DTA-CN**, as shown in **Figure 3c**. [21] In the lowest excited singlet state ($S_1$), the F1 fragment plays a critical role in facilitating electron transfer upon excitation. Both **DBT-CN** and **DBF-CN** exhibit similar levels of electron transfer contribution, ranging from approximately 39.1% to 40.3%, indicating significant involvement of the F1 fragment in these processes. However, in the $S_2$ excited state, the electron transfer contribution from F1 to F2 decreases markedly to between 25.5% and 26.7%. This reduction suggests that the electron transfer pathway is predominantly driven by the $S_1$ state, with both $S_1$ and $S_2$ states exhibiting pronounced local excitation (LE) characteristics, implying that excitation remains largely localized within the fragments. In contrast, the **DTA-CN** compound shows a higher electron transfer contribution in the $S_1$ state, reaching 44.8%, highlighting a more prominent role of the F1 fragment in the electron

transfer process for this compound. Notably, in the $S_2$ state, there is no observable electron transfer from the F1 fragment to the F2 fragment; instead, electron transfer occurs internally within the F1 fragment, specifically between the triphenylamine and triphenyltriazine units. This unique behavior indicates that for **DTA-CN**, the $S_1$ state serves as the sole pathway for electron transfer, underscoring the distinct electronic characteristics of this compound compared to **DBT-CN** and **DBF-CN**.

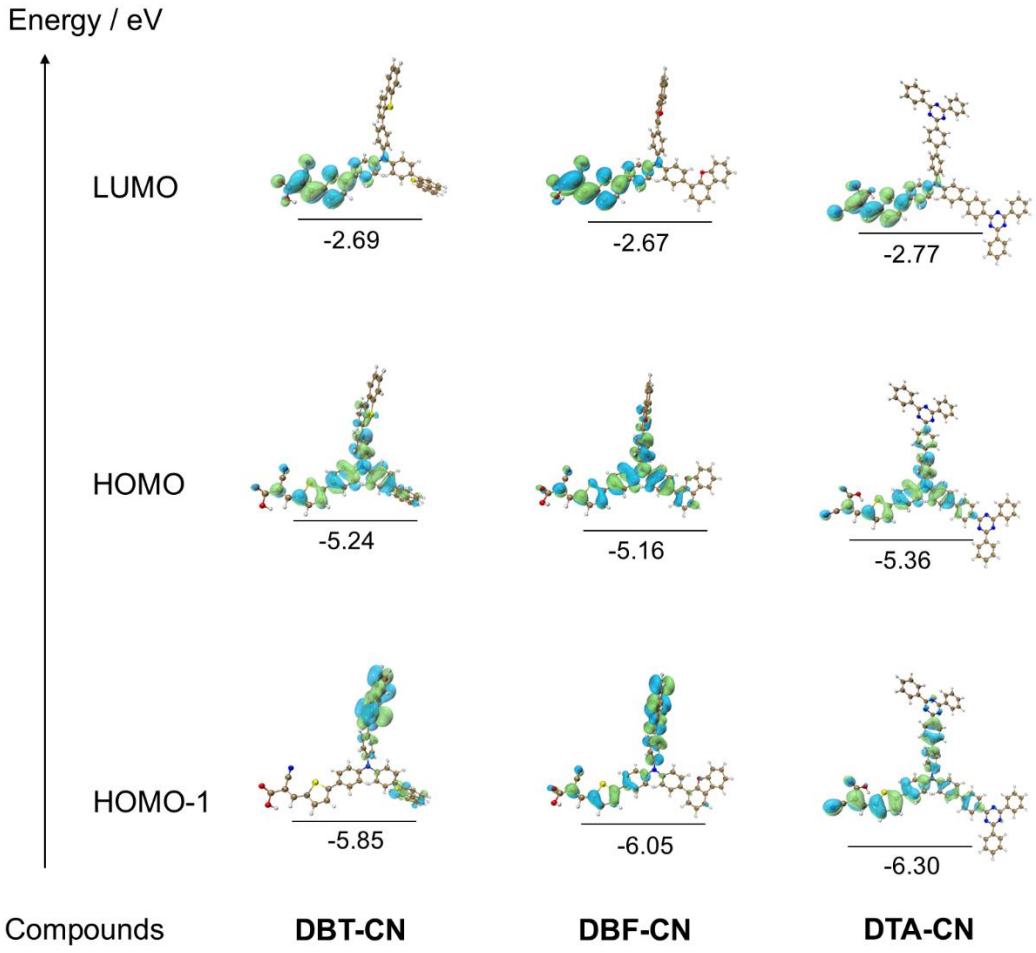


**Figure 2.** The optimized configurations and frontier molecular orbitals of PSs derivatives, computed by DFT with a B3LYP/6–31G(d) basis using the Gaussian 09 program.

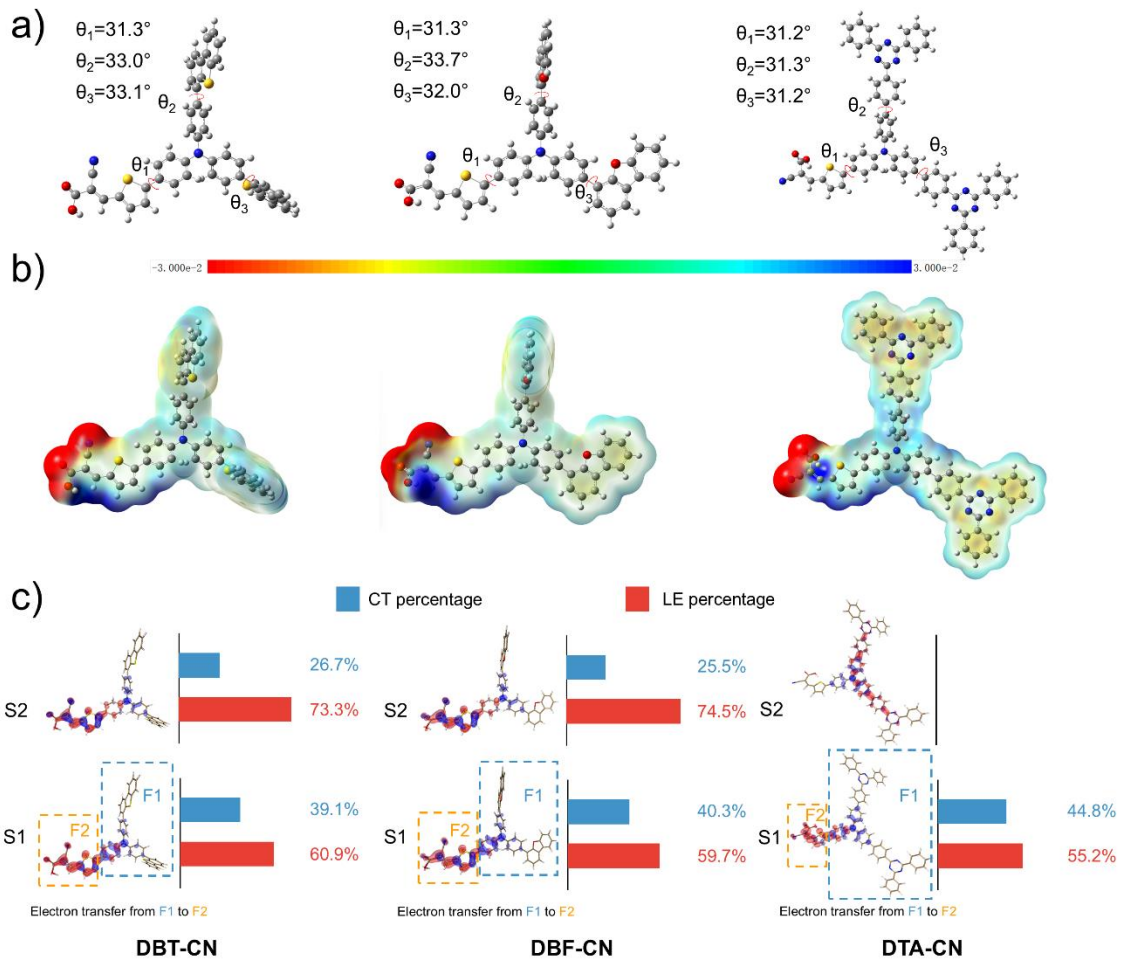


**Figure 3.** (a) The calculated molecular configuration; (b) electrostatic potential surface maps; c) Hole-particle distribution (hole: blue; particle: red) with IFCT analysis and excited state energy alignment of PSs.

### 2.3 Photophysical properties

The absorption and emission spectra of PS derivatives in dichloromethane are shown in **Figure 4**, with key parameters summarized in **Table 1**. All PSs exhibit three main absorption bands ranging from 300 to 600 nm. The absorption band at 300 nm is attributed to local π-π* transitions within the aromatic rings, while the band at 350 nm is due to the π-π* transitions of TPA [22]. The broad absorption peaks from 400 to 600 nm are the result of the extended conjugation of DBT and DBF, which enhance intramolecular charge transfer (ICT) from the electron-donating segment to the electron-accepting anchoring groups [23,24]. **DBT-CN** and **DBF-CN** display similar

absorption characteristics. In contrast, **DTA-CN** shows a red-shifted broad absorption peak at 400 nm, attributed to the extensive conjugated structure of the triphenyltriazine group, along with a weaker CT peak at 500 nm. All the target PSs exhibit high ε at 470 nm (the emission λ of blue LED), measured at 27,000, 37,000, and 16,500 $cm^{-1}M^{-1}$ for **DBT-CN**, **DBF-CN**, and **DTA-CN**, respectively. At 520 nm (the emission λ of green LED), the ε range from 8,900 to 29,000 $mol^{-1}$ $cm^{-1}$. This range is comparable to other reported D-π-A PSs [25–27] and single-anchor organic dyes [28–30]. Moreover, to elucidate the absorption properties of dye-adsorbed $TiO_2$ samples, UV-Vis diffuse reflectance spectra (UV-Vis DRS) tests were carried out (**Figure 4c**). The three dye-adsorbed $TiO_2$ samples displayed features akin to those observed in a dichloromethane solution. They exhibited a broad red-shifted absorption peak within the 400-600 nm range, allowing the photocatalyst to capture light in the visible spectrum. Thus, they can be conveniently excited by commercial LEDs.

All three PSs exhibit photoluminescence (PL) in dichloromethane at room temperature. **DBT-CN** and **DBF-CN** emit red PL, with peaks at 648 and 663 nm, respectively, while **DTA-CN** shows green PL, peaking at 553 nm, and demonstrates strong fluorescence characteristics.

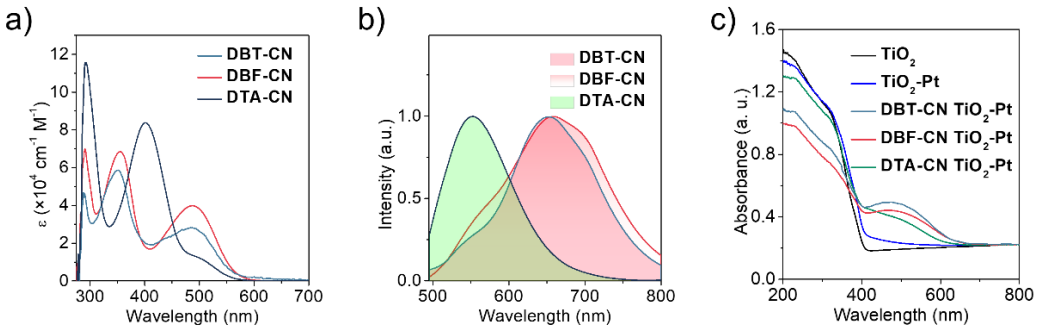


**Figure 4.** (a) UV/Vis absorption spectra of **DBT-CN**, **DBF-CN** and **DTA-CN** in $CH_2Cl_2$ at 293 K; (b) Normalized photoluminescence spectra of **DBT-CN**, **DBF-CN** and **DTA-CN** in $CH_2Cl_2$ at 293 K; (c) UV-Vis diffuse reflectance spectra of **$TiO_2$**, **$TiO_2$-Pt**, **DBT-CN $TiO_2$**, **DBF-CN $TiO_2$-Pt** and **DTA-CN $TiO_2$-Pt**.

**Table 1.** Optical properties of the PSs measured in $CH_2Cl_2$ solution ($1.0 \times 10^{-5}$ M)

| PS | $\lambda_{abs}$ (nm) | $\varepsilon$ ($cm^{-1}M^{-1}$) | $\lambda_{PL}$ (nm) |
|---|---|---|---|
| **DBT-CN** | 288; 352; 488 | 45723; 58702; 28030 | 650 |
| **DBF-CN** | 289; 354; 488 | 69326; 68588; 39677 | 663 |
| **DTA-CN** | 291; 401; 498 | 115485; 84218; 12392 | 553 |

### 2.4 Electrochemical properties

The first oxidation potentials ($E_{ox}$) for these compounds, which correspond to their HOMO energy levels ($E_{HOMO}$), were measured against a standard $Ag/Ag^+$ reference electrode, as shown in **Table 2** and **Figure S19.** As shown in **Figure S19a**, the reference potential of ferrocene is at 0.68 V, the $E_{ox}$ values were found to be 1.19 V for **DBT-CN**, 1.06 V for **DBF-CN**, and 1.13 V for **DTA-CN**. These values translate to $E_{HOMO}$ levels of –5.25 eV, –5.12 eV, and –5.19 eV, respectively. Notably, these $E_{HOMO}$ levels are significantly more negative than the redox potential of ascorbic acid (AA), which is –4.65 eV at approximately pH 4[31]. This indicates that the PSs have a strong thermodynamic driving force for regeneration from their oxidized states during photocatalytic processes, such as water-splitting. The zero-zero excitation energy ($E_{0\text{-}0}$), which represents the energy gap between the HOMO and the LUMO, was calculated from absorption spectra [26,32]. The $E_{0\text{-}0}(E_g)$ values for **DBT-CN**, **DBF-CN**, and **DTA-CN** are 2.22 eV, 2.22 eV, and 2.24 eV, respectively (**Figure S18**). These values provide insight into the electronic transitions and the efficiency of light absorption by the dyes. The LUMO energy levels ($E_{LUMO}$) for **DBT-CN**, **DBF-CN**, and **DTA-CN** were calculated to be –3.03 eV, –2.9 eV, and –2.95 eV, respectively. These $E_{LUMO}$ values are higher than the conduction band edge of $TiO_2$, which is approximately –4.0 eV [33]. The more negative conduction band of $TiO_2$ compared to the $E_{LUMO}$ of the PSs facilitates efficient electron injection from the excited PSs into the $TiO_2$, enhancing charge separation. This efficient charge separation is crucial for improving the photocatalytic activity, as it provides a stronger driving force for the subsequent chemical reactions

involved in processes like photocatalytic water-splitting [34].

Electrochemical impedance spectroscopy (EIS) was conducted on all the PSs using a typical transmission line model to evaluate their charge recombination and charge transfer resistance. The Nyquist plots for PSs **DBT-CN**, **DBF-CN**, and **DTA-CN** are shown in **Figure S20b**. The arc radii follow the order **DTA-CN** > **DBF-CN** > **DBT-CN**, indicating that **DBT-CN** and **DBF-CN** have lower charge recombination resistance at the interface compared to **DTA-CN**, thereby enhancing interfacial electron transfer. Furthermore, photocurrent measurements were employed to assess the stability of the PSs and the effectiveness of charge separation. [35] During light on/off tests, a rapid and consistent photocurrent response indicates stable photocatalytic activity, while higher photocurrent density suggests efficient charge separation. [36] The measurement was conducted following established procedures. [37] **Figure S20a** shows the photocurrent response of the PSs over six on/off cycles under visible light, clearly demonstrating their electron transfer efficiency and confirming stable photocatalytic activity. Notably, **DBT-CN** and **DBF-CN** exhibit significantly higher photocurrent intensity upon illumination, which gradually decreases over time. This trend suggests superior charge separation efficiency and enhanced hydrogen generation capability.

**Table 2**. Electrochemical Data and Energy Levels for **DBT-CN**, **DBF-CN** and **DTA-CN**.

| PS | $E_{ox}$/V[a] | $E_{HOMO}$/eV[b] | $E_{0\text{-}0}$/eV[c] | $E_{ox*}$/V[d] | $E_{LUMO}$/eV[e] |
|---|---|---|---|---|---|
| **DBT-CN** | 1.19 | –5.25 | 2.22 | –1.03 | –3.03 |
| **DBF-CN** | 1.06 | –5.12 | 2.22 | –1.16 | –2.90 |
| **DTA-CN** | 1.13 | –5.19 | 2.24 | –1.11 | –2.95 |

[a] Onset of first oxidation potentials were measured by cyclic voltammetry in dichloromethane ($CH_2Cl_2$) solution containing 0.1 M of $NBu_4PF_6$ against $Ag/Ag^+$ reference electrode, with glassy carbon working electrode and platinum wire auxiliary electrodes.

[b] Calculated from -($E_{ox}$+4.71-0.64), as reversible oxidation of ferrocene was $E_{1/2}$ = 0.09 V and the $E_{HOMO}$ of ferrocene is equal to -4.80 eV vs. to vacuum level.

[c] $E_{0\text{-}0}$ was determined from the onset of absorption spectrum. at the corresponding lowest energy absorption maxima.

[d] $E_{OX*} = E_{OX} – E_{0\text{-}0}$.

[e] $E_{LUMO} = E_{HOMO} + E_{0\text{-}0}$.

## 2.5 Photocatalytic Hydrogen Production Study

Owing to the excellent light-harvesting ability of PSs in the 350-550 nm range, they show great potential in photocatalytic hydrogen evolution. To develop a visible-light-driven water-splitting photocatalytic system, we first loaded Pt nanoparticles onto commercial $TiO_2$ nanoparticles using the method described in the reference [38]. Subsequently, the composite materials were treated with a PSs solution to adsorb the dye onto the $TiO_2$-Pt composites. Previous studies have shown that this approach can enhance the efficiency and stability of hydrogen production [39,40]. After centrifuging to recover the PS-adsorbed $TiO_2$-Pt composites, the amount of dye remaining in the solution was negligible, indicating that PS was fully adsorbed onto the $TiO_2$-Pt nanoparticles. The percentage of dye loading on $TiO_2$-Pt was also evaluated by monitoring the change in absorbance of the dye solution before and after adsorption, as shown in **Figure S21**. The results indicated that the adsorption rate for all PSs was approximately 96-98%. The photocatalytic performance of PS-adsorbed $TiO_2$-Pt composites was studied in a 5 mL 0.8 M ascorbic acid (AA) aqueous solution (pH 4.0), with AA serving as a sacrificial agent, under blue or green LED irradiation. Comparing the reaction mixtures before and after irradiation, the AA solution changed from colorless to deep yellow. This change is attributed to the formation of dehydroascorbic acid during the PS regeneration process in photocatalysis [41]. Furthermore, by comparing the PS photocatalytic reaction mixtures before and after irradiation, the $TiO_2$ composites retained their original color. This indicates that in our study [39], issues such as dye desorption [42] and PS photobleaching were not observed.

**Figure 5** depicts the hydrogen production fitting curves for three PSs, along with the corresponding data (TON, TOF, $TOF_i$, $Activity_i$, and $AQY_i$%) tabulated in **Table 3**. Within the initial 48 hours, there is a notable rise in hydrogen production for all the PSs. **DBT-CN** sustains significant hydrogen production activity under both blue and green light irradiation. The **DBF-CN** photocatalytic system exhibits the most remarkable activity under green light, producing 8.0 mL of hydrogen after 48 hours, with a TON of 5303, and reaching a hydrogen yield of 15.3 mL after 258 hours. In contrast, the activity

of **DTA-CN** notably decreases after 100 hours. The outcomes from **DBF-CN** are akin to the most efficient and stable photocatalytic water-splitting systems incorporating photosensitizers singly attached to $TiO_2$ molecules, as documented in literature employing organic PSs under green light, while comparing TOF and TON values (**Table S1**)[26,43,44]. Finally, we selected **DBF-CN**, which exhibited the best performance under green light, to study its hydrogen production efficiency under different pH conditions (**Figure S22** and **Table S2**). Within 48 hours, the hydrogen production at pH 3 and pH 4 reached relatively high volumes of 8.3 mL and 8.0 mL, respectively. Conversely, at pH 5 and pH 6, only 3.2 mL and 3.5 mL hydrogen were produced. This disparity can be attributed to the heightened efficacy of ascorbic acid in resisting photodegradation induced by UV-visible light in more acidic environments, thus more efficiently fostering hydrogen production.[45] The different sensitization behaviors of PSs on $TiO_2$-Pt as photocatalysts can be explained from both photophysical and theoretical calculation standpoints. It is worth noting that the ε of **DBT-CN**, **DBF-CN**, and **DTA-CN** showcase notable variances in the blue light wavelength range, yet this evidently is not the primary factor influencing photocatalytic hydrogen production. From the theoretical perspective of IFCT, **DTA-CN** only has the $S_1$ state as the sole excited singlet state for charge transfer from the F1 fragment to F2, while the $S_2$ state involves ICT within the F1 fragment without charge transfer to F1. In contrast, **DBT-CN** and **DBF-CN**, despite possessing a lower CT ratio in the $S_2$ state, demonstrate a propensity for charge transfer to the F2 fragment. Both **DBT-CN** and **DBF-CN** exhibit high ε in the green light range, showcasing high hydrogen production performance under green light irradiation, sustaining hydrogen evolution for more than 258 hours. This indicates that the PSs exhibit robust photostability and are not easily desorbed from $TiO_2$, leading to a slow degradation/desorption process. Additionally, it is crucial to highlight that all systems exhibit notable stability and limited photobleaching capability.

In summary, the analysis indicates that in the triphenylamine-thiophene single-anchor photocatalytic system, enhancing the electron cloud density of the triphenylamine group can more effectively induce a red shift in the absorption spectrum. This creates multiple energy level channels for electron transfer. Furthermore, it also suggests that

incorporating the donor on the triphenylamine group ($D_2$-D-π-A) is more effective in enhancing hydrogen production efficiency compared to introducing the acceptor ($A_2$-D-π-A).

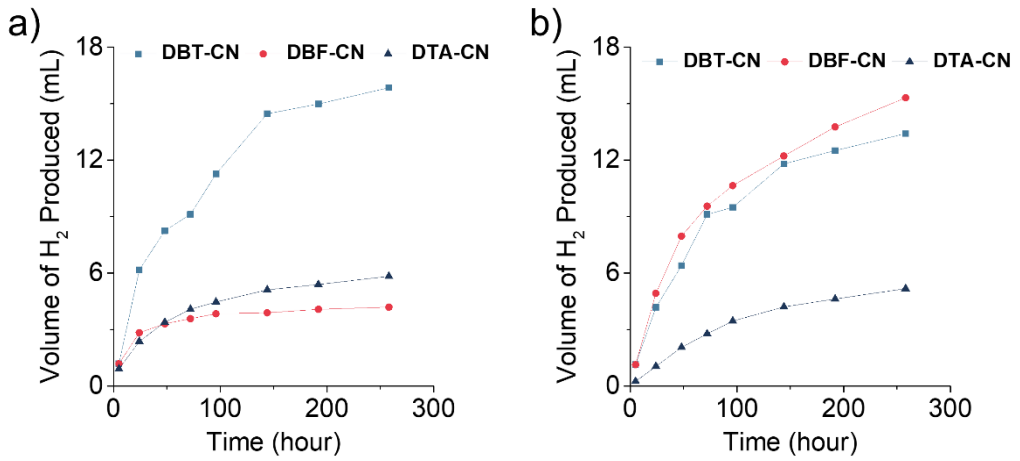


**Figure 5.** Kinetic traces of hydrogen generation by different photosensitizers (**DBT-CN**, **DBF-CN** and **DTA-CN**) under the irradiation of a) blue LED (472 nm) and b) green LED (520 nm). Each sample flask contained 0.8M ascorbic acid (5 mL) in water (pH 4.0) and 20 mg PS–$TiO_2$–Pt sample.

**Table 3**. Light-Driven hydrogen Generation Data with PSs **DBT-CN**, **DBF-CN** and **DTA-CN** on $TiO_2$–Pt.

| Dye | $H_2$(mL) | TON [a] | TOF ($h^{-1}$) [b] | $TOF_i$ ($h^{-1}$) [c] | $Activity_i$ (μmol $g^{-1}$ $h^{-1}$) [d] | $AQY_i$% [e] |
|---|---|---|---|---|---|---|
| **Irradiation under blue LED (472 nm) for 48 h** | | | | | | |
| **DBT-CN** | 8.3<br>15.9<br>(258 h) | 5498<br>10555 | 45.4<br>87.2 | 158.1 | 118383 | 0.79 |
| **DBF-CN** | 3.3 | 2203 | 18.2 | 158.0 | 118268 | 0.79 |
| **DTA-CN** | 3.4 | 2258 | 18.7 | 121.3 | 90815 | 0.61 |
| **Irradiation under green LED (520 nm) for 48 h** | | | | | | |
| **DBT-CN** | 6.4<br>13.4<br>(258 h) | 4261<br>8933 | 35.2<br>73.8 | 152.6 | 114262 | 0.76 |
| **DBF-CN** | 8.0<br>15.3<br>(258 h) | 5303<br>10202 | 43.8<br>84.3 | 151.6 | 113532 | 0.76 |
| **DTA-CN** | 2.1 | 1370 | 11.3 | 36.9 | 27594 | 0.18 |

| | | | |
|---|---|---|---|
| | 5.2 (258 h) | 3448 | 28.5 |

[a] Turnover number of $H_2$ is calculated as 2 x number of moles of $H_2$ produced divided by the number of mole of PS attached to platinized $TiO_2$.
[b] Turnover frequency is calculated per hour (48h).
[c] Initial turnover frequency in the first 5 h.
[d] Initial photocatalytic activity of the system is defined as number of micromoles of $H_2$ evolved per gram of platinum loaded per hour.
[e] Initial apparent quantum yield percentage ($AQY_i$ %) of the system.

## 3. Conclusion

In summary, a series of new $D_2$-D-π-A and $A_2$-D-π-A organic photosensitizers based on the framework of (Z)-2-cyano-3-(5-(4-(diphenylamino)phenyl)thiophen-2-yl)acrylic acid molecular framework was successfully synthesized and characterized. The pathways of their excited-state electron transfer can be modulated by varying the electron-donating and -withdrawing abilities on the triphenylamine moiety. Experimental results showed that **DBT-CN** exhibited excellent performance under both blue and green light, while **DBF-CN** achieved the highest hydrogen production performance under green light, with a TON of 10,202, an initial $TOF_i$ of 151.6 $h^{-1}$, $Activity_i$ of 113,532 μmol $g^{-1}h^{-1}$, and an AQY% of 0.76%. Further theoretical calculations of IFCT demonstrated that **DTA-CN** has only a single charge transfer pathway in the $S_1$ singlet excited state, resulting in its lower hydrogen production efficiency under illumination. These findings establish **DBF-CN** as one of the most effective and long-lasting photosensitizers for the photocatalytic production of hydrogen, especially when paired with molecular Pt-$TiO_2$, under the irradiation of green LED. Compared to the $A_2$-D-π-A system, the $D_2$-D-π-A system enhances PHE while maintaining stability under prolonged illumination. This work provides valuable insights for designing high-performance organic photosensitizers for sustainable hydrogen production.

## 4. Experimental Sections

### 4.1 Materials and Reagents.

All chemical reactions were conducted under nitrogen atmosphere with Schlenk line techniques. All glassware was cleaned and dried in oven before use. The commercially available reagents were used without further purification unless specified. These reagents were purchased from Sigma-Aldrich, Acros Organics, Tokyo Chemical Industry Co. Ltd. (TCI), Dieckmann, J&K Scientific or Macklin. Solvents were dried by distillation with respective drying agents. All the reactions were monitored by thin-layer chromatography (TLC) using silica gel coated aluminum plates from Merck.

### 4.2 Instrumentation

$^{1}$H and $^{13}$C NMR (Nuclear Magnetic resonance) spectra were measured in DMSO-*d* or chloroform-*d*, with tetramethylsilane (TMS) exploited as an internal standard for chemical shift calibration, on the Bruker Advance-III 400 MHz FT-NMR System. The integration and labelling of peaks were performed by the Bruker NMR Software Suite. Mass spectra were collected by Agilent 6540 Liquid Chromatography-Electrospray Ionization Quadrupole-Time-of-Flight (ESI-QTOF) Mass Spectrometer. Ultraviolet–visible spectra were obtained by Varian Cary 4000 of UV-Visible Spectrophotometer at 293 K, with the samples dissolved in dichloromethane. Photoluminescence spectra were acquired by Agilent G9800 AA Cary Eclipse (Type II) of Fluorescence Spectrophotometer at 293 K, with the samples dissolved in dichloromethane. Fluorescence lifetimes of the PSs were determined by the Photon Technology International (PTI) QuantaMaster 50 Steady-state Spectrofluorometer at 293 K. The Marquardt-based non-linear least-squares fitting routine was adopted for analyzing the decay curves. Those curves were presented in a single-exponential function, regarding the $I= I_0 + A \exp(-t/\tau)$. Cyclic voltammetry was performed on the CHI 630C Electrochemical Analyzer/Workstation, with the scan rate of 100 mV $s^{-1}$. The experiments were performed in dichloromethane solution, using the three-electrode cell with a 3 mm glassy carbon working electrode, an aqueous Ag/AgCl reference electrode, and a platinum counter electrode. 0.1 M tetrabutylammonium hexafluorophosphate was used as the supporting electrolyte, while ferrocene was applied as internal standard,

such that the corresponding one-electron oxidation potential could be measured. The electrochemical impedance spectroscopy (EIS) was operated in a three-electrode system, in which the carbon rod and Ag/AgCl electrode were used as counter and reference electrode respectively, with 0.1 M KCl solution was used as electrolyte. The samples were dispersed in a mixture solvent of 1 mL methanol and 0.1 mL nafion solution with a mass of 1 mg. The prepared sample was dripped on the platinum carbon electrode and EIS data was collected by applying a sine wave with an amplitude of 50 mV over a frequency range from 100000 Hz to 0.01 Hz on a CHI 760 electrochemical workstation.

### 4.3 Synthesis of Materials

**5-(4-(diphenylamino)phenyl)thiophene-2-carbaldehyde (1)** [46]

4- (Diphenylamino)phenylboronic acid (2.89 g, 10 mmol, 1 equiv) was dissolved in 30 mL THF in one-necked round-bottom flask with rapid stirring, followed by the addition of 5-Bromothiophene-2-carbaldehyde (2.28 g, 12 mmol, 1.2 equiv) and potassium carbonate (4.14 g, 30 mmol, 3 equiv) (aq, 2M). The reaction mixture was degassed thoroughly by freeze-pump-thaw cycle at least 3 times before tetrakis(triphenylphosphine)palladium(0) (0.231 g, 0.201 mmol, 0.02 equiv) was added. The mixture was heated to reflux at 85 $^{o}$C under nitrogen atmosphere for 8 hours. After quenching the reaction by the addition of water (50 mL), the reaction mixture was extracted with ethyl acetate and brine, the organic layer was collected and dried over $Na_2SO_4$. The solvent was removed by rotary evaporator with reduced pressure, while the crude product was purified with column chromatography, filled with silica gel and eluted with hexane/dichloromethane (*v/v* 2:1). The target product was dried and was obtained as yellow solid. The purified product was a yellow solid (yield: 2.545 g, 71.7%). $^{1}$H NMR (400 MHz, Chloroform-*d*) δ 9.85 (s, 1H), 7.71 (d, $J$ = 4.0 Hz, 1H), 7.53 – 7.50 (m, 2H), 7.32 – 7.27 (m, 5H), 7.16 – 7.04 (m, 8H).

**5-(4-(bis(4-bromophenyl)amino)phenyl)thiophene-2-carbaldehyde (2)**

Compound **1** (0.8 g, 2.250 mmol, 1equiv ) was dissolved in 5 mL dry DMF, followed by adding the NBS (0.961 mg, 5.4 mmol, 2.4 equiv) in portions at 0 ºC and stirred for 1 hour. The reaction mixture was stirred overnight at room temperature under nitrogenic atmosphere. The mixture was quenched with D.I. water and was then extracted with dichloromethane and brine, followed by drying over the $Na_2SO_4$. The solvent was removed by rotary evaporator with reduced pressure, while the product was further purified with column chromatography, filled with silica gel and washed with hexane/dichloromethane (*v/v* 6:1). The purified product was dried by rotary evaporator and was found to be a pale-yellow solid (yield: 0.929 g, 81%). $^1$H NMR (400 MHz, Chloroform-*d*) δ 9.87 (s, 1H), 7.72 (d, *J* = 4.0 Hz, 1H), 7.56 – 7.53 (m, 2H), 7.41 – 7.38 (m, 4H), 7.32 (d, *J* = 3.9 Hz, 1H), 7.07 – 7.04 (m, 2H), 7.01 – 6.97 (m, 4H).

**5-(4-(bis(4-(dibenzo[b,d]thiophen-4-yl)phenyl)amino)phenyl)thiophene-2-carbaldehyde (3)**

**Compound 2** (1.024 g, 2 mmol, 1 equiv ) was dissolved in 12 mL THF and 2 mL water in one-necked round-bottom flask with rapid stirring, followed by the addition of dibenzothiophene-4-boronic acid (1.094 g, 4.8 mmol, 2.4 equiv) and potassium carbonate (1.656 g, 12 mmol, 6 equiv ) (aq, 2M). The reaction mixture was degassed thoroughly by freeze-pump-thaw cycle at least 3 times before tetrakis(triphenylphosphine)palladium (0) (0.092 g, 0.08 mmol, 0.04 equiv) was added. The mixture was heated to reflux at 85 °C under nitrogen atmosphere for 8 hours. After quenching the reaction by the addition of water (50 mL), the reaction mixture was extracted with ethyl acetate and brine, the organic layer was collected and dried over $Na_2SO_4$. The solvent was removed by rotary evaporator with reduced pressure, while the crude product was purified with column chromatography, filled with silica gel and eluted with hexane/dichloromethane (v/v 1:3). The target product was dried and was obtained as yellow solid. The purified product was a yellow solid (yield: 813.9 mg, 56.6%). $^1$H NMR (400 MHz, Chloroform-*d*) δ 9.88 (s, 1H), 8.22 – 8.14 (m, 4H), 7.89 – 7.84 (m, 2H), 7.77 – 7.71 (m, 5H), 7.64 (d, *J* = 8.3 Hz, 2H), 7.57 (dd, *J* = 15.7, 8.1 Hz, 3H), 7.52 – 7.46 (m, 5H), 7.39 – 7.34 (m, 5H), 7.29 (d, *J* = 8.4 Hz, 2H). $^{13}$C NMR

(151 MHz, Chloroform-*d*) δ 182.73, 154.40, 146.60, 141.57, 139.52, 138.35, 137.80, 136.38, 136.33, 135.93, 135.83, 129.42, 127.52, 126.88, 126.77, 125.21, 124.94, 124.46, 123.67, 123.19, 122.64, 121.80, 120.39. Found: [M+H]+ 720.1504, 'molecular formula C47H29NOS3' requires [M+H]+ 720.1484.

**5-(4-(bis(4-(dibenzo[b,d]furan-4-yl)phenyl)amino)phenyl)thiophene-2-carbaldehyde (4)**

**Compound 2** (1.024 g, 2 mmol, 1 equiv ) was dissolved in 12 mL THF and 2 mL water in one-necked round-bottom flask with rapid stirring, followed by the addition of Dibenzofuran-4-boronic acid (1.017 g, 4.8 mmol, 2.4 equiv) and potassium carbonate (1.656 g, 12 mmol, 6 equiv ) (aq, 2M). The reaction mixture was degassed thoroughly by freeze-pump-thaw cycle at least 3 times before tetrakis(triphenylphosphine)palladium (0) (0.092 g, 0.08 mmol, 0.04 equiv) was added. The mixture was heated to reflux at 85 ℃ under nitrogen atmosphere for 8 hours. After quenching the reaction by the addition of water (50 mL), the reaction mixture was extracted with ethyl acetate and brine, the organic layer was collected and dried over $Na_2SO_4$. The solvent was removed by rotary evaporator with reduced pressure, while the crude product was purified with column chromatography, filled with silica gel and eluted with hexane/dichloromethane (v/v 1:3). The target product was dried and was obtained as yellow solid. The purified product was a yellow solid (yield: 1016.7 mg, 74.0%). $^{1}$H NMR (400 MHz, Chloroform-*d*) δ 9.88 (s, 1H), 8.22 – 8.15 (m, 4H), 7.88 – 7.84 (m, 2H), 7.76 – 7.71 (m, 5H), 7.66 – 7.62 (m, 2H), 7.60 – 7.52 (m, 4H), 7.50 – 7.46 (m, 4H), 7.38 – 7.34 (m, 5H), 7.32 – 7.28 (m, 2H). $^{13}$C NMR (151 MHz, Chloroform-*d*) δ 182.73, 156.15, 153.29, 146.43, 141.50, 131.77, 129.86, 129.67, 128.97, 127.46, 127.29, 126.93, 126.46, 125.16, 125.01, 125.00, 124.61, 124.22, 123.49, 123.32, 123.13, 122.85, 120.74, 119.51, 111.87. Found: [M+H]+ 687.2030, 'molecular formula C47H29NO3S' requires [M+H]+ 687.1868.

**5-(4-(bis(4'-(4,6-diphenyl-1,3,5-triazin-2-yl)-[1,1'-biphenyl]-4-yl)amino)phenyl)thiophene-2-carbaldehyde (5)**

**Compound 2** (1.024 g, 2 mmol, 1 equiv ) was dissolved in 12 mL THF and 2 mL water in one-necked round-bottom flask with rapid stirring, followed by the addition of 2,4-Diphenyl-6-[4-(4,4,5,5-tetramethyl-1,3,2-dioxaborolan-2-yl)phenyl]-1,3,5-triazine (2.089 g, 4.8 mmol, 2.4 equiv) and potassium carbonate (1.656 g, 12 mmol, 6 equiv ) (aq, 2 M). The reaction mixture was degassed thoroughly by freeze-pump-thaw cycle at least 3 times before tetrakis (triphenylphosphine)palladium (0) (0.092 g, 0.08 mmol, 0.04 equiv) was added. The mixture was heated to reflux at 85 ℃ under nitrogen atmosphere for 8 hours. After quenching the reaction by the addition of water (50 mL), the reaction mixture was extracted with ethyl acetate and brine, the organic layer was collected and dried over $Na_2SO_4$. The solvent was removed by rotary evaporator with reduced pressure, while the crude product was purified with column chromatography, filled with silica gel and eluted with hexane/dichloromethane (v/v 1:1). The target product was dried and was obtained as yellow solid. The purified product was a yellow solid (yield: 950.6 mg, 49.0%). $^1$H NMR (400 MHz, Chloroform-*d*) δ 9.87 (s, 1H), 8.86 – 8.77 (m, 13H), 7.83 – 7.79 (m, 4H), 7.73 (d, *J* = 4.0 Hz, 1H), 7.70 – 7.66 (m, 4H), 7.61 (td, *J* = 7.4, 6.9, 3.6 Hz, 14H), 7.35 (d, *J* = 4.0 Hz, 1H), 7.32 – 7.30 (m, 3H), 7.25 – 7.22 (m, 2H). $^{13}$C NMR (151 MHz, Chloroform-*d*) δ 182.73, 171.65, 171.37, 146.78, 144.30, 137.79, 136.28, 135.61, 134.97, 132.56, 129.59, 129.00, 128.69, 128.35, 127.50, 126.87, 125.12, 123.62, 123.24. Found: [M+H]+ 970.3347, 'molecular formula C65H43N7OS' requires [M+H]+ 970.3323.

**(E)-3-(5-(4-(bis(4-(dibenzo[b,d]thiophen-4-yl)phenyl)amino)phenyl)thiophen-2-yl)-2-cyanoacrylic acid (DBT-CN)**

Compound 3 (0.100 g, 0.138 mmol, 1equiv) was dissolved in 5 mL anhydrous THF, followed by the addition of cyanoacetic acid (35.42 mg, 0.412 mmol, 3 equiv) and piperidine (0.33 mL, 0.3 mmol). The reaction mixture was stirred at reflux under nitrogenous atmosphere overnight. The reaction was quenched with adding water, and then extracted with dichloromethane and brine, followed by drying over the $Na_2SO_4$. The solvent was removed by rotary evaporator with reduced pressure, while the product was further purified with column chromatography, filled with silica gel and washed

with dichloromethane, followed by dichloromethane. The purified product was an orange solid (yield: 0.093 g, 86%). $^1$H NMR (400 MHz, DMSO-d6) δ 8.50 (s, 1H), 8.45 – 8.37 (m, 4H), 8.07 – 8.00 (m, 3H), 7.81 (dd, J = 8.7, 2.5 Hz, 6H), 7.72 (d, J = 4.0 Hz, 1H), 7.67 – 7.60 (m, 4H), 7.54 (dt, J = 7.1, 3.6 Hz, 4H), 7.36 (d, J = 8.2 Hz, 4H), 7.24 (d, J = 8.6 Hz, 2H). [M-H]- 785.1360, 'molecular formula C50 H30 N2 O2 S3' requires [M-H]- 785.1397.

**(E)-3-(5-(4-(bis(4-(dibenzo[b,d]furan-4-yl)phenyl)amino)phenyl)thiophen-2-yl)-2-cyanoacrylic acid (DBF-CN)**

**Compound 4** (0.100 g, 0.146 mmol, 1equiv) was dissolved in 5 mL anhydrous THF, followed by the addition of cyanoacetic acid (35.42 mg, 0.412 mmol, 3 equiv) and piperidine (0.33 mL, 0.3 mmol). The reaction mixture was stirred at reflux under nitrogenous atmosphere overnight. The reaction was quenched with adding water, and then extracted with dichloromethane and brine, followed by drying over the $Na_2SO_4$. The solvent was removed by rotary evaporator with reduced pressure, while the product was further purified with column chromatography, filled with silica gel and washed with dichloromethane, followed by dichloromethane. The purified product was an orange solid (yield: 0.092 g, 84%). $^1$H NMR (400 MHz, DMSO-$d_6$) δ 8.49 (s, 1H), 8.41 (dd, $J$ = 12.6, 6.9 Hz, 4H), 8.03 (q, $J$ = 3.9 Hz, 3H), 7.81 (d, $J$ = 8.1 Hz, 6H), 7.71 (d, $J$ = 4.3 Hz, 1H), 7.65 – 7.60 (m, 4H), 7.54 (dd, $J$ = 6.0, 3.2 Hz, 4H), 7.35 (d, $J$ = 8.2 Hz, 4H), 7.23 (d, $J$ = 8.2 Hz, 2H). [M+H]+ 757.5449, 'molecular formula C47H29NOS3' requires [M+H]+ 757.204.

**(Z)-3-(5-(4-(bis(4'-(4,6-diphenyl-1,3,5-triazin-2-yl)-[1,1'-biphenyl]-4-yl)amino)phenyl)thiophen-2-yl)-2-cyanoacrylic acid (DTA-CN)**

**Compound 5** (0.05 g, 0.052 mmol, 1equiv) was dissolved in 5 mL anhydrous THF, followed by the addition of cyanoacetic acid (13.14 mg, 0.154 mmol, 3 equiv) and piperidine (0.33 mL, 0.3 mmol). The reaction mixture was stirred at reflux under nitrogenous atmosphere overnight. The reaction was quenched with adding water, and then extracted with dichloromethane and brine, followed by drying over the $Na_2SO_4$.

The solvent was removed by rotary evaporator with reduced pressure, while the product was further purified with column chromatography, filled with silica gel and washed with dichloromethane, followed by dichloromethane. The purified product was an orange solid (yield: 0.048 g, 90 %). $^{1}$H NMR (400 MHz, Chloroform-d) δ 8.86 (d, J = 5.1 Hz，5H), 7.94 (d, J = 4.3 Hz, 1H), 7.82 – 7.77 (m，17H), 7.75 – 7.63 (m，14H), 7.54 (d, J = 5.1 Hz，5H), 7.35 (d, J = 5.1 Hz，1H). Found: [M+H]+ 1035.9933, 'molecular formula C68 H44 N8 O2 S' requires [M-H]- 1035.3235.

### 4.4 Preparation of platinized titanium (IV) oxide (Pt-$TiO_2$)

The 0.5 wt-% platinized $TiO_2$ was prepared by adding 1.6 g $TiO_2$ nanopowder (anatase, 99.7% trace metal basis, particle size <25 nm, from Sigma Aldrich) and 0.1 mL $H_2PtCl_6$ (8 wt-%) solution into 40 mL methanol. The grey slurry was stirred vigorously under the radiation from a mercury-coated lamp (300W, HF300PD, EYE Lighting) for 24 hours. The greyish crude product was purified by washing with methanol and centrifugation (3500 rpm, 5 minutes) for thrice. The Pt-$TiO_2$ was then dried in vacuum oven at 60 ºC for 8 hours. The surface disorder phenomenon and microstructure of Pt/$TiO_2$ were examined using Scanning Electron Microscope (SEM). A typical image obtained is shown in **Figure S22a**, where the platinum particles appear non-clustered and exhibit heterogeneity. To investigate the crystal structure of the Pt/$TiO_2$ samples, XRD measurements were conducted, as shown in **Figure 22b**. For pure $TiO_2$, nine distinct peaks were observed at 25.3°, 37.9°, 48.0°, 54.0°, 55.2°, 62.8°, 68.7°, 70.4°, and 75.3°. According to JCPDS 21-1272, these peaks correspond to the anatase $TiO_2$ planes of (101), (004), (200), (105), (211), (101), (116), (220), and (215), respectively. [47] In the Fourier Transform Infrared Spectroscopy (FTIR) spectrum, signal peaks were also observed at 564 $cm^{-1}$, 1636 $cm^{-1}$, and 3417 $cm^{-1}$.[48] To further explore the chemical states of Pt and surface oxygen species, X-ray photoelectron spectroscopy (XPS) studies were conducted on catalytic cracking ions with different interface perimeters. The Pt 4f spectrum can be deconvoluted into two doublets centered at binding energies (B.E.) of 71.8, 72.77, and 75.1 eV (with a doublet separation of 3.3 eV for Pt $4f_{7/2}$ and

Pt $4f_{5/2}$). The Pt species in all catalysts exist in the proportions of approximately 31.2% $Pt^0$, 30.1% $Pt^{2+}$, and 38.7% $Pt^{4+}$, as shown in **Figure 22d**. [49]

### 4.5 Preparation of the dye-loaded platinized titanium(IV) oxide

The prepared Pt-$TiO_2$ (20 mg) was added to 2.5 mL (50 μM) PS-dissolved dichloromethane solution, followed by sonicating thoroughly at 20 $^oC$ for 30 minutes. The $TiO_2$ nanoparticles would turn from grey to pale purple-red and distributed in the colored milky solution. The solution mixture was then centrifuged at 3500 rpm for 10 minutes to reclaim the nanoparticles by removing the colorless supernatant and drying under vacuum in dark overnight. The dried pellet would be directly used for the photocatalytic hydrogen evolution experiment. The collected supernatant was used for estimating the dye-loading percentage for each PS separately by comparing absorbance differences before and after the dye adsorption of their low-energy peaks and have included the calculation results of dye-loading about 6.25 μmol/g. These carboxylate-anchoring dyes were favorably attached onto the $TiO_2$ surfaces and yielded close to 100% adsorption. The corresponding UV/vis absorption spectra of dyes before and after adsorbing onto Pt-$TiO_2$ are illustrated in **Figure S23**.

### 4.6 Photocatalytic hydrogen evolution studies

The experiments were conducted by adding the dye-loaded $TiO_2$-Pt pellet (~20 mg) and 5 mL aquatic ascorbic acid (0.8 M) solution at pH 4.0, acting as SED for regenerating the PSs, into a 25 mL pear-shaped flask. AA was chosen because of its well-studied relationship between hydrogen generation efficiency and pH and its illustrious redox reactions [50]. The sealed pear-shaped flask was then purged with a gas mixture of nitrogen/methane (80:20 mol%) for 10 minutes. The presence of methane was important as it served as the internal standard for the gas chromatography (GC) analysis for every trial. The reaction mixture would be stirred rapidly at 20 $^oC$ with the blue (*ca.* 472 nm) or green (*ca.* 520 nm) light-emitting diodes (LED) under the just-fit container which blocked-out the environmental stray light and prevent the loss of scattered light

from the LEDs. Powers of the LED were measured by a power meter (Model: BIM-7001, Hangzhou Brolight Technology Co., Ltd.) with a thermal sensor (Model: BIM-7203-0100F). The measured power was ~80 mW for each reaction flask. At each time point, the headspaces of each flask were detected by the GC (Shimadzu GC-8A with 5Å molecular sieve column, and a TCD detector) to determine the volume of hydrogen produced, based on the peak area ratio of hydrogen: methane with reference to the calibration curve (**Figure S24**). The time points taken were 5, 24, 48, 72, 96, 144, 192, 256 hours from independent reaction flasks (duplicate for each sample) for **DBF-CN, DBT-CN** and **DTA-CN** and blank (Pt-$TiO_2$). The blue/green LED irradiation was assumed to be monochromatic with emission intensity maximum at 472/520 nm for calculating the initial apparent quantum yield ($AQY_i$%) for each sample dye. The performance of PHE was also presented in terms of turnover number (TON), turnover frequency (TOF), initial turnover frequency ($TOF_i$) and initial photocatalytic activity ($Activity_i$) to evaluate the photocatalytic systems' ability in generating hydrogen. The equations are showed as follow:[51]

$$TON = \frac{no.of\ moles\ of\ H_2\ produced\ x2}{no.of\ moles\ of\ PS\ adsorned\ onto\ PtTiO_2}$$

$$TOF = \frac{TON}{hours\ of\ irradiation}$$

$$TOF_i = \frac{TON\ of\ the\ first\ time\ point}{hours\ of\ irradiation\ of\ the\ first\ time\ point}$$

$$Activity_i = \frac{\frac{no.of\ micromole\ of\ H_2\ generated}{grams\ of\ Pt\ loaded}}{no.of\ hours}$$

$$AQY_i\% = \frac{rate\ of\ H_2\ produced\ x2}{rate\ of\ incident\ photons}\ x100\%$$

### 4.7 Theoretical calculation

The ground state geometries were optimized using the density functional theory (DFT) method, specifically the B3LYP functional at the 6-31g(d) basis set level. HOMO/LUMO, hole-electron analysis,[52] and interfragment charge transfer (IFCT) analysis were conducted using Multiwfn 3.8,[53] and visualizations were performed with

the VMD program based on the output files from TD-DFT calculations.

## Conflict of Interest

The authors declare no conflict of interest.

## Acknowledgements

This work was supported by the Hong Kong Research Grants Council (PolyU 123021/17P), Environment and Conservation Fund (ECF 86/2021) from the Government of HKSAR and the Hong Kong Polytechnic University (ZVVU and ZVXU) for their financial support.

## Reference


[1] A. Kumar, P. Daw, Milstein, D. Milstein, *Chem. Rev.* **2022**, 122, *1*, 385–441.

[2] M. G. Schultz, T. Diehl, G. P. Brasseur, W. Zittel, *Science* **2003**, 302, 624-627

[3] S. Nishioka, F. E. Osterloh, X. Wang, T. E. Mallouk, K. Maeda, *Nat. Rev. Methods Primers* **2023**, *3*, 1, 42.

[4] A. Fujishima, K. Honda, *Nature* **1972**, *238* ,5358, 37–38.

[5] S. Jeong, K.-H. Chung, H. Lee, H. Park, K.-J. Jeon, Y.-K. Park, S.-C. Jung, *ACS Sustainable Chem. Eng.* **2017**, *5*, 5, 3659–3666.

[6] H. Ding, D. Zha, S. Han, Jiang, N. Jiang, *J. Taiwan Inst. Chem. Eng.* **2023**, *151*, 105135.

[7] Y. Li, M.-Q. Zhang, Y.-F. Liu, Y.-X. Sun, Q.-H. Zhao, T.-L. Chen, Y.-F. Chen, S.-F. Wang, *Nanomaterials* **2022**, *12*, 7, 1122.

[8] R. Ghamarpoor, A. Fallah, M. Jamshidi, *Sci. Rep.* **2023**, *13* (1), 9793.

[9] F. Kwaku Asiam, A. Kumar Kaliamurthy, Md. Mahbubur Rahman, B. Yadagiri, C. Chen, H. Cheol Kang, M. Sadiq, J. Ryu, A. Ewusi Mensah, M. Zain Qamar, K. Yoo, J.-J. Lee, *Coord. Chem. Rev.* **2024**, *514*, 215908.

[10] F. A. Faraghally, A. F. Musa, C. Chen, Y. Chen, Y. Chen, C. Yeh, T. Wei, *Small Struct.* **2024**, *5*, 11, 2400236.

[11] M. Jiang, R. Wang, Z. Deng, G. Xu, Q. Shangguan, L. Sun, L. Zhang, X. Yang, *ACS Appl. Mater. Interfaces* **2024**, *16*, 38, 51265–51273.

[12] F. Xu, T. T. Testoff, L. Wang, X. Zhou, *Molecules* **2020**, *25*, 19, 4478.

[13] C. Han, S. Xiang, P. Xie, P. Dong, C. Shu, C. Zhang, J. Jiang, *Adv. Funct. Mater.* **2022**, *32* (16), 2109423.

[14] M. Chen, J. Xiong, Q. Shi, T. Li, X. Li, Y. Feng, B. Zhang, *Chem. Eng. J.* **2023**, *475*, 146099.

[15] X. Xia, J. Feng, Z. Zhong, X. Yang, N. Li, D. Chen, Y. Li, Q. Xu, J. Lu, *Adv. Funct. Mater.* **2024**, *34* (13), 2311987.

[16] H. Shang, Q. Li, K. Jiang, X. Zhan, *J. Energy Chem.* **2016**, *25* (4), 615–620.

[17] C. Rodríguez-Seco, M. Méndez, C. Roldán-Carmona, R. Pudi, M. K.

Nazeeruddin, E. J. Palomares, *Angew. Chem. Int. Ed.* **2020**, *59* (13), 5303–5307.

[18] X. Xiao, J. Hu, Z. Huo, J. Liang, B. Yang, X. Hong, Z. Chen, Y. Wang, C. Li, Y. Zheng, *Adv. Opt. Mater.* **2024**, 2401754.

[19] A. Fabiańczyk, P. Gnida, P. Chulkin, S. Kula, M. Filapek, A. Szlapa-Kula, H. Janeczek, E. Schab-Balcerzak, *Solar Energy* **2021**, *220*, 1109–1119.

[20] Y. Wu, W. Zhu, *Chem. Soc. Rev.* **2013**, *42* (5), 2039–2058.

[21] X. Tang, L.-S. Cui, H.-C. Li, A. J. Gillett, F. Auras, Y.-K. Qu, C. Zhong, S. T. E. Jones, Z.-Q. Jiang, R. H. Friend, L.-S. Liao, *Nat. Mater.* **2020**, *19* (12), 1332–1338.

[22] Y. Wen, H. Xiang, X. Luo, S. Ji, J. Zhao, J. Zhao, H.-L. Zhang, W.-C. Chen, Y. Huo, *Dyes Pigm.* **2022**, *205*, 110551.

[23] J. Ramakrishna, P. Venkatakrishnan, *Chem. Asian J.* **2017**, *12* (2), 181–189.

[24] A. Thangthong, N. Prachumrak, R. Tarsang, T. Keawin, S. Jungsuttiwong, T. Sudyoadsuk, V. Promarak, *J. Mater. Chem.* **2012**, *22* (14), 6869.

[25] D. P. Hagberg, J.-H. Yum, H. Lee, F. De Angelis, T. Marinado, K. M. Karlsson, R. Humphry-Baker, L. Sun, A. Hagfeldt, M. Grätzel, Md. K. Nazeeruddin, *J. Am. Chem. Soc.* **2008**, *130* (19), 6259–6266.

[26] J. Huang, Y. Lei, L. Xiao, X. Chen, Y. Zhong, S. Qin, J. Liu, *ChemSusChem* **2020**, *13* (5), 1037–1043.

[27] P.-Y. Ho, Y. Wang, S.-C. Yiu, Y.-Y. Kwok, C.-H. Siu, C.-L. Ho, L. T. Lin Lee, T. Chen, *J. Photoch. Photobio. A* **2021**, *406*, 112979.

[28] N. Manfredi, B. Cecconi, V. Calabrese, A. Minotti, F. Peri, R. Ruffo, M. Monai, I. Romero-Ocaña, T. Montini, P. Fornasiero, A. Abbotto, *Chem. Commun.* **2016**, *52* (43), 6977–6980.

[29] C.-Y. Lo, D. Kumar, S.-H. Chou, C.-H. Chen, C.-H. Tsai, S.-H. Liu, P.-T. Chou, K.-T. Wong, *ACS Appl. Mater. Interfaces* **2016**, *8* (41), 27832–27842.

[30] B. Cecconi, N. Manfredi, R. Ruffo, T. Montini, I. Romero-Ocaña, P. Fornasiero, A. Abbotto, *ChemSusChem* **2015**, *8* (24), 4216–4228.

[31] X. Li, J. Yu, J. Low, Y. Fang, J. Xiao, X. Chen, *J. Mater. Chem. A* **2015**, *3* (6), 2485–2534.

[32] S. A. Haque, E. Palomares, B. M. Cho, A. N. M. Green, N. Hirata, D. R. Klug, J. R. Durrant, *J. Am. Chem. Soc.* **2005**, *127* (10), 3456–3462.

[33] S. E. Skrabalak, Y. Xia, *ACS Nano* **2009**, *3* (1), 10–15.

[34] J. Yu, J. Jin, B. Cheng, M. Jaroniec, *J. Mater. Chem. A* **2014**, *2* (10), 3407.

[35] Y. Liu, Z. Liu, C. Guo, T. Chen, C. Guo, Y. Lu, J. Wang, *Appl. Surf. Sci.* **2022**, *571*, 151284.

[36] D. Jiang, W. Wang, S. Sun, L. Zhang, Y. Zheng, *ACS Catal.* **2015**, *5* (2), 613–621.

[37] J. Tang, R.Guo, W. Zhou, C. Huang, W. Pan, *Appl. Catal. B* **2018**, *237*, 802–810.

[38] J. M. Herrmann, J. Disdier, P. Pichat, *J. Phys. Chem.* **1986**, *90* (22), 6028–6034.

[39] B. Zheng, R. P. Sabatini, W.-F. Fu, M.-S. Eum, W. W. Brennessel, L. Wang, D. W. McCamant, R. Eisenberg, *Proc. Natl. Acad. Sci. U.S.A.* **2015**, *112* (30).

[40] P.-Y. Ho, C.-H. Siu, W.-H. Yu, P. Zhou, Chen, T. Chen,C.-L. Ho, L. T. L. Lee, ; Y.-H. Feng, J. Liu, K. Han, Y. H. Lo, W.-Y. Wong, *J. Mater. Chem. C* **2016**, *4* (4), 713–726.

[41] Y. Wen, C.-L. Ho, S. Huang, Y. Y. Kwok, S. Huang, *Renew. Energ.* **2024**, *237*, 121728.

[42] T. Le, M. S. Akhtar, D. M. Park, J. C. Lee, O.-B. Yang, *Appl. Catal. B* **2012**, *111–112*, 397–401.

[43] H. Yang, S. K. Kamarudin, L. J.Minggu, M. Kassim, *Renew. Sust. Energ. Rev.* **2015**, *43*, 599–610.

[44] T. Lazarides, T. McCormick, P. Du, G. Luo, B. Lindley, *J. Am. Chem. Soc.* **2009**, *131* (26), 9192–9194.

[45] K. Aguilar, A. Garvín, A. V. Lara-Sagahón, A. Ibarz, *Food Chem.* **2019**, *297*, 124864.

[46] Y. Gao, S. Dai, J. Zhu, L. Wu, L. Han, Y. Li, Q. Ye, Y. Cui, *J. Photochem. Photobiol. A* **2023**, *438*, 1144563

[47] A. Tiwari, N. Duvva, V. N. Rao, S. M. Venkatakrishnan, L. Giribabu, U. Pal, *J. Phys. Chem. C* **2019**, *123* (1), 70–81.

[48] A. E. Mragui, O. Zegaoui, I. Daou, J. C. G. E. Da Silva, *Environ. Sci. Pollut.* **2021**, *28*, 25130–25145.

[49] A. Lu, H. Sun, N. Zhang, L. Che, S. Shan, J. Luo, J. Zheng, L. Yang, D.-L. Peng, C.-J. Zhong, B. Chen, *ACS Catal.*, **2019**, 9, 7431–7442

[50] M. Natali, *ACS Catal.* **2017**, *7* (2), 1330-1339.

[51] B. Cecconi,N. Manfredi, T. Montini, P. Fornasiero, A. Abbotto, *Eur. J. Org. Chem.* **2016,** (31), 5194-5215.

[52] Z. Liu, T. Lu, Q. Chen, *Carbon* **2020**, *165*, 461–467.

[53] T. Lu, F. Chen, *J. Comput. Chem.* **2012**, *33*, 580–592.

# Table of Contents

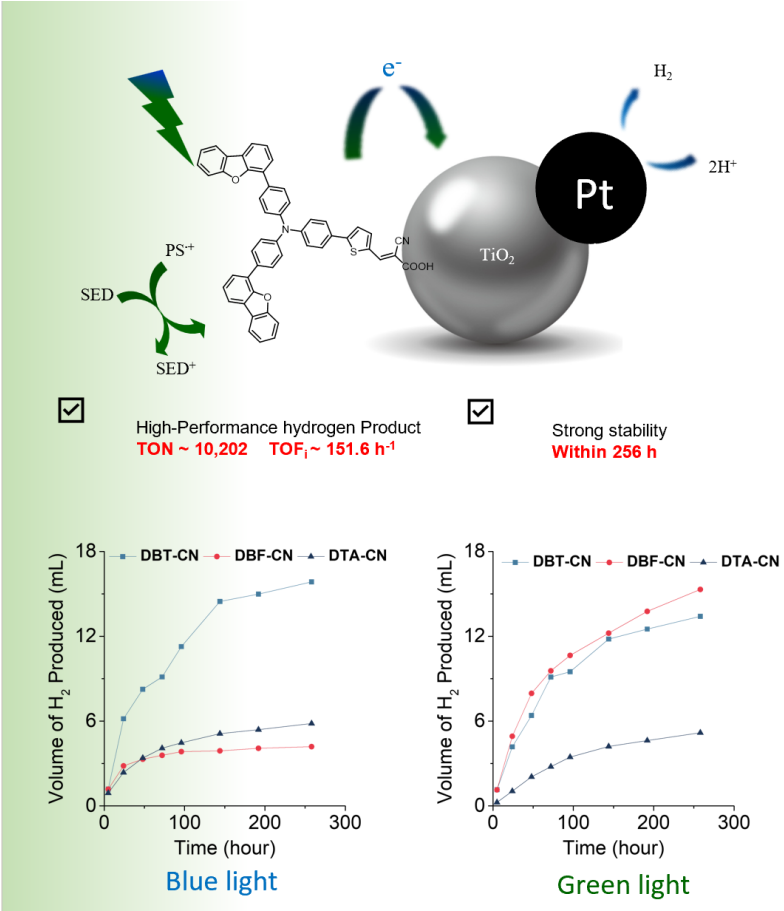


New organic photosensitizers, with a triphenylamine-based molecular framework, were synthesized and characterized. The **DBT-CN** dye showed an impressive turnover number of 10,555 and an initial turnover frequency of 152.6 $h^{-1}$ under green light. The (donor)$_2$-donor-π-acceptor design outperformed the (acceptor)$_2$-donor-π-acceptor configuration in photocatalytic hydrogen evolution, remaining stable after prolonged light exposure.

Twitter: The Hong Kong Polytechnic University